

A 1-to-8 Fully Modular Stacked SIW Antenna Array for Millimeter-Wave Applications

This paper was downloaded from TechRxiv (<https://www.techrxiv.org>).

LICENSE

CC BY-NC-SA 4.0

SUBMISSION DATE / POSTED DATE

11-01-2022 / 19-07-2022

CITATION

Segura-Gómez, Cleofás; Palomares-Caballero, Ángel; Padilla, Pablo (2022): A 1-to-8 Fully Modular Stacked SIW Antenna Array for Millimeter-Wave Applications. TechRxiv. Preprint.
<https://doi.org/10.36227/techrxiv.18134057.v2>

DOI

[10.36227/techrxiv.18134057.v2](https://doi.org/10.36227/techrxiv.18134057.v2)

Copyright:

©2022 IEEE. Personal use of this material is permitted. Permission from IEEE must be obtained for all other uses, in any current or future media, including reprinting/republishing this material for advertising or promotional purposes, creating new collective works, for resale or redistribution to servers or lists, or reuse of any copyrighted component of this work in other works.

Disclaimer:

This work has been published on *IEEE Transactions on Antennas and Propagation*. DOI: 10.1109/TAP.2022.3191324

A 1-to-8 Fully Modular Stacked SIW Antenna Array for Millimeter-Wave Applications

Cleofás Segura-Gómez, Ángel Palomares-Caballero, and Pablo Padilla

Abstract—This paper presents a vertically stacked SIW antenna array that enables different array configurations with the minimum number of SIW layers. This achievement lies in the modular feature offered by the proposed design. Specifically, 4 distinct array configurations can be produced with only 3 different design of SIW layers. Depending on the number of SIW layers employed in the stacked antenna, the directivity in the E-plane is modified. To obtain an equal and in-phase power distribution among the array elements, H- and E-plane corporate feeding networks are efficiently implemented in each array configuration. Array configurations of 1, 2, 4 and 8 radiating layers are offered by the proposed modular array, where each radiating layer is formed by 8 H-plane horn antennas. The simulated directivity for the array configurations ranges from 15.8 dBi to 23.8 dBi and the main beam direction remains fixed along the operating frequency range. The array design has been manufactured and agreement between simulated and measured results are observed. The measured impedance bandwidth in all the array configurations is from 35 GHz to 41 GHz (15.79% bandwidth) with a reduction in the E-plane beamwidth as the number of radiating layers increases.

Index Terms—Antenna array, millimeter waves, modularity, SIW.

I. INTRODUCTION

FOR next generation communication systems, there will be an increase in their frequency due to the need to avoid saturated sub-6 GHz bands and achieve higher bandwidths. However, the increase in frequency is also an engineering challenge because the propagation losses grow. The solutions usually proposed are the reduction of communication links, for example, introducing femtocells [1]; and/or using high directivity antennas to efficiently radiate power [2], [3].

Since the target operating frequencies will be in the millimeter-wave range, the technology used to design the antenna must provide transmission efficiency, be low cost and with a profile as low as possible. One of the technologies that meets mostly these requirements is the substrate integrated waveguide (SIW) [4]. Several antenna arrays have been developed in this waveguide technology for millimeter-wave applications [5], [6]. One of the most interesting possibility that offers the SIW is the easy layer stacking to produce multilayer antenna arrays. This design strategy has been used to make different antenna designs at millimeter frequencies [7]–[9].

Thanks to the feasibility already shown in the literature of making antennas by stacking SIW layers, an advance in this design approach is to provide modularity. The meaning of modular is that depending on the number of plates stacked, the characteristics of the antenna are different, and always using the highest number of common layers. Modular designs have been used for 2-D phased antenna array design where each antenna or subarray of antennas is fed independently [10], [11]. Depending the number of modular antennas are used or the type of modular antenna, different directivity values [11] or

This work was supported in part by the Spanish Government under Project PID2020-112545RB-C54, in part by “Junta de Andalucía” under Project B-TIC-402-UGR18, Project A-TIC-608-UGR20, Project P18.RT.4830 and Project PYC20-RE-012-UGR, and in part by the Predoctoral Grants FPU20/00256 and FPU18/01965. (Corresponding author: Cleofás Segura-Gómez.)

C. Segura-Gómez, Á. Palomares-Caballero, and P. Padilla are with the Departamento de Teoría de la Señal, Telemática y Comunicaciones, Universidad de Granada, 18071 Granada, Spain (email: cleofas@ugr.es; angelpc@ugr.es; pablopadilla@ugr.es)

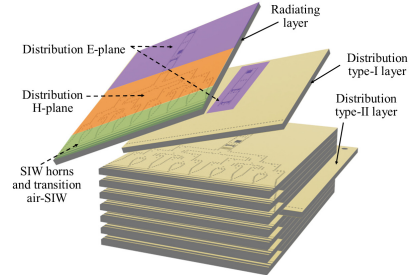


Fig. 1. Design of the proposed fully modular antenna array. The array configuration illustrated is the higher one in terms of stacked antenna elements.

bandwidth [10] can be achieved. Instead of modularity in a horizontal plane as presented in the previous works, vertical modularity has also been reported in the literature [12], [13] to produce phased array with endfire radiation. However, the possible connection between the different stacked layers becomes more complex. On the other hand, the modularity in passive antenna arrays has been hardly explored. In [14], a vertical stacking of leaky-wave antennas has been presented to enhance the directivity in the E-plane. Nevertheless, the leakage of each antenna has to be adjusted to obtain a uniform feeding along the array which hampers modularity. The antenna design proposed in [15] achieves a certain degree of modularity by stacking in the E-plane several SIW H-plane horn antennas. A series coaxial feeding is employed in this array but this strategy does not provide uniform and in-phase feeding for the array elements and thus, the main beam is tilted and scanned with the frequency.

In this paper, we present a fully modular design of a SIW antenna array stacked in the E-plane. The antenna design provides 4 array configurations with the only use of 3 different types of SIW layers. Depending on the directivity desired for the application or coverage needed, an array configuration is adopted. In addition, due to the fact that the array configurations share layers, this leads to a saving in mass production. To the best of the authors’ knowledge, it is the first time that modularity is implemented in an SIW passive antenna array providing different directivity in the E-plane with fixed radiating direction. Fig. 1 shows the design of the proposed modular array. The configuration illustrated in the figure corresponds to an array configuration that provides the highest directivity because the antenna array is composed by 8 radiating layers. Additionally, only two types of distribution layers are needed to obtain equal power distribution from the input port for the four array configurations mentioned above.

II. ANTENNA ARRAY DESIGN

The substrate employed for all the designed SIW layers is the commercial RO4003C with double metallized cladding of annealed copper ($\sigma = 5.8 \cdot 10^7$ S/m). The height h_0 of the substrate is 1.524 mm with a relative permittivity ϵ_r of 3.55 and tabulated loss tangent $\tan\delta$ of 0.0027 (@10 GHz). By setting a width w_0 for the SIW waveguide equal to 3.2 mm and following the general SIW design equations to avoid leakage losses from 32 GHz to 44 GHz, the periodicity between metallized vias d and the vias radius r are 0.8

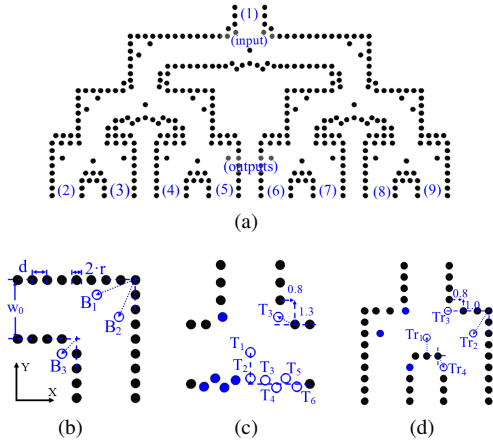


Fig. 2. (a) Layout of the H-plane corporate feeding network and its fundamental components: (b) SIW 90° bend, (c) SIW -3 dB T-splitter, and (d) -3 dB compact SIW T-splitter. The blue unfilled vias show the modified or introduced vias and the blue filled vias are the symmetrical vias. The dimensions of the bend are: $B_{1X} = 2.1$, $B_{1Y} = 0.8$, $B_{2X} = 0.9$, $B_{2Y} = 2$, and $B_{3X} = B_{3Y} = 0.8$. The dimensions of the T-splitter are: $T_{1Y} = 1.7$, $T_{2Y} = T_{5Y} = 0.3$, $T_{3Y} = 0.2$, $T_{4Y} = T_{6Y} = -0.2$, $T_{3X} = 0.8$, $T_{4X} = 1.4$, $T_{5X} = 1.9$, and $T_{6X} = 2.5$. The dimensions of the compact T-splitter are: $Tr_{1Y} = 1.3$, $Tr_{2X} = Tr_{3X} = 1.1$, $Tr_{2Y} = 1.6$, $Tr_{4X} = 0.4$, and $Tr_{4Y} = 0.8$. Dimensions in mm.

mm and 0.25 mm, respectively. In the following subsections, each component that composes the antenna array is described and its simulated performance is discussed. All the simulations presented in the paper have been performed with CST Studio Suite.

A. H-plane corporate feeding network and antenna element

In this first subsection, it is presented the H-plane corporate feeding network that is implemented in the radiating layer (see Fig. 1). This type of corporate feeding network has been used in other works but for our design, the bends and power splitters have been designed to cover the target frequency range with a very low reflection coefficient (-20 dB). In this manner, the possible mismatch will be minimized when all the fundamental components are joined together to form the corporate feeding network. The designed feeding network considers one SIW input port and eight SIW output ports which will correspond to the antenna input ports. In order to distribute the electromagnetic (EM) field from the input port to outputs ports, three levels of two-by-two divisions are needed as is illustrated in Fig. 2(a). In the design process, it is important to take into account the distance between the centers of the outputs because they will determine the distance between antenna centers. Therefore, in order to avoid grating lobes and preserve high directivity for the radiating layer, this distance is 5.6 mm. The fundamental components that forms the H-plane corporate feeding network are the 90° waveguide bend, the -3 dB T-splitter and, the compact design of a T-splitter with waveguide bends. Their layouts are illustrated in Figs. 2(b), 2(c) and, 2(d), respectively. The T-splitters with waveguide bends are needed in the last splitting level to ensure the distance between centers of the output ports.

In the layout of the fundamental components (Figs. 2(b), 2(c) and, 2(d)), some vias are highlighted in blue since they are very important to achieve a high performance in the scattering parameters (S-parameters). The S-parameters of the depicted fundamental components are displayed in Figs. 3(a), 3(b), and 3(c). All of them show a reflection coefficient $|S_{11}|$ similar or lower than -20 dB from 35 GHz to 42 GHz. Complementary, the transmission coefficient $|S_{21}|$ is almost the ideal value for all the designs but with some losses due to the presence of the dielectric in the SIW. Once the fundamental elements of the corporate feeding network are designed with the

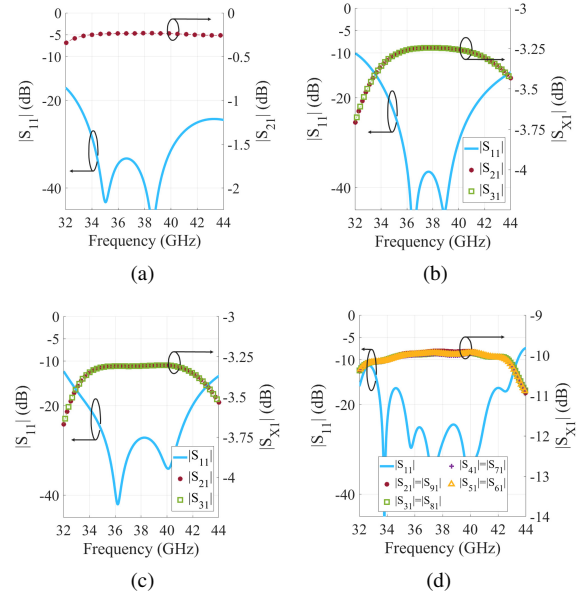


Fig. 3. $|S|$ -parameters of H-plane components: (a) SIW 90° bend, (b) SIW -3 dB T-splitter, (c) -3 dB compact SIW T-splitter, and (d) Complete.

expected performance, all of them are joined to form the final design of the H-plane corporate feeding network shown in Fig. 2(a) and the S-parameters of it in the Fig. 3(d). Thanks to the adequate individual performance of the fundamental components, the global performance of the H-plane corporate feeding network maintains a low reflection coefficient in the desired frequency band. This causes a uniform and in-phase feeding through the output ports. As it was observed for the transmission coefficient of the fundamental components, the transmission coefficients of the complete feeding network are a little bit far from the ideal ones due to the dielectric losses.

At the end of each of the eight outputs of the H-plane corporate feeding network, the radiating elements are implemented. These are SIW H-plane horns whose design is shown in Fig. 4. Its aperture is set by the distance between array elements. For a proper impedance matching between SIW and free space, a transition is employed [15]. In order to use efficiently the geometrical space between SIW horns, the last vias of each SIW horn are shared with the neighboring antennas. In Fig. 4, it is presented the $|S_{11}|$ and the directivity, taking into account mutual coupling through a periodic environment at antenna sides. A proper impedance matching is achieved on the target frequency band with a directivity of 6.7 dBi at the center frequency.

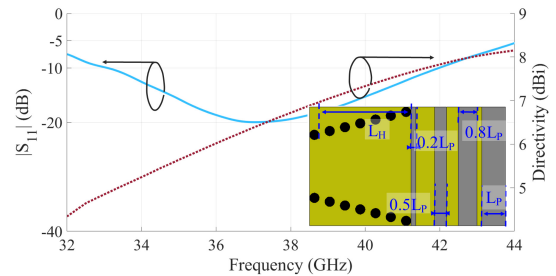


Fig. 4. SIW H-plane horn: Top view, $|S_{11}|$ and directivity. Dimensions are: $L_H = 4.9$ mm, and $L_P = 1.2$ mm.

B. Modular E-plane corporate feeding network

This subsection is devoted to describe the waveguide components implemented in the distribution type-I layer (see Fig. 1). This SIW

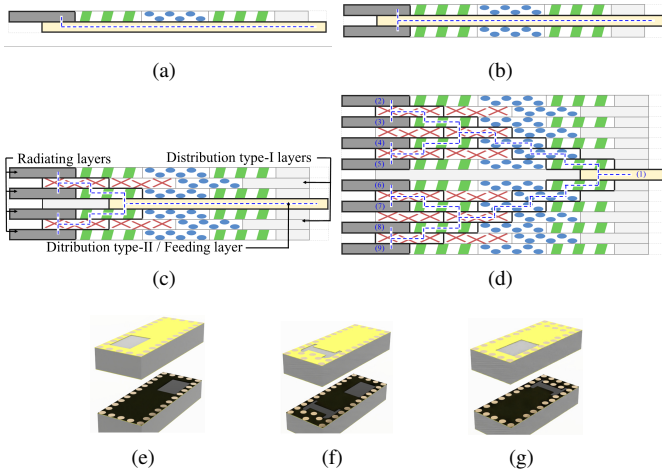


Fig. 5. Set of array configurations: (a) 1 radiating layer, (b) 2 radiating layers, (c) 4 radiating layers, and, (d) 8 radiating layers. Waveguide components: (e) waveguide type-I, (f) waveguide type-II and, (g) waveguide type-III. In each waveguide component, it is shown the top and the bottom views. The length of each waveguide component are 9.45 mm, 9.3 mm, and 8.35 mm, respectively. The waveguide components which are crossed by the blue dashed line subfigures (a)-(d) are the one used in each array configuration.

layer enables the uniform and in-phase feeding from the distribution type-II layer to all the stacked radiating layers. Figs. 5(a)-5(d) illustrate how the three types of SIW layers are stacked to produce all the array configurations. It is important to note that in the radiating layer it is also implemented waveguide components since in this manner, the number of different layers used to achieve all the array configurations is minimized. From left to right, the radiating layer is composed of the H-plane distribution (in gray), a waveguide type-III (in green stripes), a waveguide type-I (in blue circles) and a waveguide type-III. The distribution type-I layer is composed of two waveguides type-II (in red crosses) and a waveguide type-I. In Figs. 5(a)-5(d), the waveguide components that are crossed by the blue dashed line are the ones used in each displayed array configuration. The other waveguide components, which are not crossed by the dashed line, are included to provide modularity for the other array configurations with the fewest number of different SIW layers. The input port of the antenna array is always located at the distribution type-II layer (in yellow) and at both sides of this layer, the radiating and distribution type-I layers are vertically stacked to produce the desired array configuration. A 3-D view of each waveguide component employed in Figs. 5(a)-5(d) is presented in Figs. 5(e)-5(g). They are SIW of certain length whose ends present coupling apertures with a particular geometry. Geometrical details are shown in Figs. 6(a) and 6(b). These coupling apertures allow the power distribution towards an upper and/or a lower SIW layer of the array, respectively. The waveguide type-I uses the coupling aperture illustrated in Fig. 6(a) which corresponds to rectangular coupling aperture located near one of the lateral walls of the SIW to enhance EM coupling. The S-parameters of this waveguide component is presented in Fig. 7(a) where it can be observed the satisfactory impedance matching along the desired bandwidth. For the waveguide type-II, whose geometrical details are in Fig. 6(b), a modified version of the conventional dog-bone coupling aperture is employed. This modified dog-bone coupling aperture is etched at both copper layers in order to split the EM field from a middle SIW layer to an upper and lower SIW layers. The S-parameters of this power splitter is presented in Fig. 7(b). It can be observed the fair distribution of the input power to the output ports and the low and wideband impedance bandwidth. The waveguide

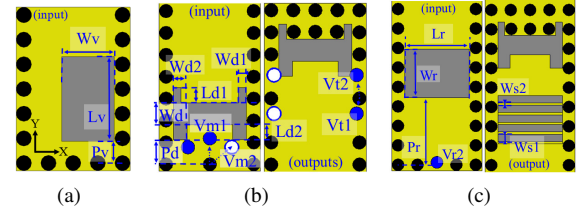


Fig. 6. Geometric details of coupling apertures used in the waveguide components: (a) rectangular coupling aperture, (b) modified dog-bone coupling aperture, and (c) fragmented rectangular coupling aperture. The dimensions of the rectangular coupling aperture are: $W_v = 1.7$, $L_v = 2.75$, and $P_v = 0.7$. The dimensions of the modified dog-bone aperture are: $W_d = 0.8$, $P_d = 1.45$, $L_{d1} = 0.55$, $L_{d2} = 0.55$, $W_{d1} = 0.3$, $W_{d2} = 0.5$, $V_{m1Y} = 0.95$, $V_{m2Y} = 0.63$, $V_{t1X} = 0.1$, $V_{t1Y} = 0.55$, $V_{t2X} = 0.1$, and $V_{t2Y} = 0.85$. The dimensions of the fragmented rectangular coupling aperture are: $W_r = 2$, $L_r = 2.7$, $P_r = 3.55$, $W_{s1} = 0.3$, $W_{s2} = 0.1$, and $V_{r2Y} = 0.1$. Dimensions in mm.

type-III is composed of the above coupling apertures which have demonstrated an adequate EM performance. The reason for using this waveguide component is for an efficient transmission between the waveguide type-I and type-II needed in the array configurations with 4 and 8 radiating layers.

In order to use the same radiating layer design for all the array configurations, the array design with a single radiating layer has to receive special attention. As it is illustrated in Fig. 5, the case with a single radiating layer differs in its feeding compared to the other configurations because it is fed by the distribution type-II layer without a power split. For the other array configurations, the radiating layers are always fed by performing a power split in either distribution type-I layer or distribution type-II layer. This fact causes the need of a waveguide component in the radiating layer that enables both feeding depending if only one radiating layer is used or if multiple radiating layers are used. For this purpose, a special waveguide component is designed and it is shown in Fig. 6(c). The waveguide component is composed by the modified dog-bone coupling aperture described above and a fragmented rectangular coupling aperture located before the dog-bone aperture. These coupling apertures are implemented in the radiating layer (named top layer in Fig. 6(c)). In the bottom layer and also the feeding layer, a rectangular coupling aperture is implemented allowing the EM coupling between rectangular apertures of both layers. The effect in this EM coupling due to the presence of the dog-bone aperture is minimal since when both layers are stacked, the dog-bone geometry is covered by the copper layer of the bottom layer. This coupling situation described above is the one referred to the case with a single radiating layer where the non-fragmented rectangular coupling aperture is implemented in the distribution type-II layer. The Fig. 7(c) shows the transmission and reflection coefficient of this waveguide component. A suitable operating bandwidth is observed from 35 GHz to 41 GHz. For the array configurations that used more than one single radiating layer, the EM coupling to the radiating layer is produced by the dog-bone coupling aperture since the bottom layer is the waveguide type-II. In these cases, the fragmented rectangular coupling aperture has minimal effect because it is covered by copper when the layers are stacked.

C. Input port

This subsection provides a description of the feeding strategy for all the array configurations. The feeding components are implemented in the distribution type-II layer (see Fig. 1). Since the targeted frequency bandwidth is in millimeter-wave frequencies and the employed waveguide technology is SIW, a wideband transition from coaxial connector (VNA ports) to SIW is designed. In addition, a commercial

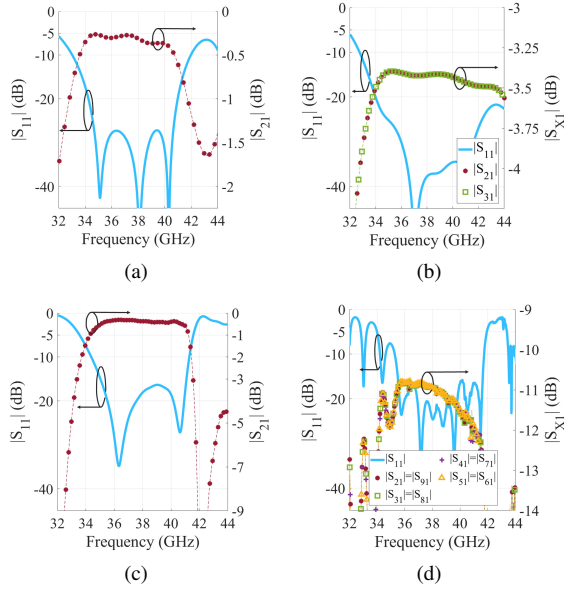


Fig. 7. $|S|$ -parameters of proposed coupling apertures shown in: (a) Fig. 6(a), (b) Fig. 6(b) and, (c) Fig. 6(c), $|S|$ -parameters of the array configuration with 8 radiating layers in magnitude.

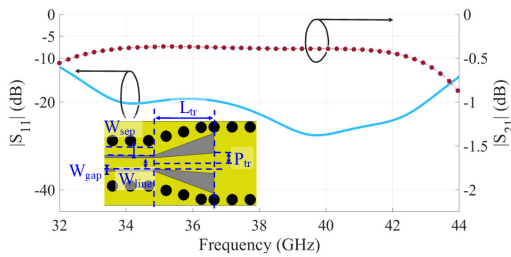


Fig. 8. Design and $|S|$ -parameters of the transition from GCPW to SIW. The dimensions are: $L_{tr} = 2.4$, $P_{tr} = 0.45$, $W_{line} = 0.5$, $W_{sep} = 0.4$, and $W_{gap} = 0.1$. Dimensions in mm.

end-launch connector 91R60918 is also utilized between the cable of the VNA and the SIW of the distribution type-II layer to ease the transition design. Taking into account the design of the end-launch connector, a grounded coplanar-waveguide (GCPW) to SIW transition has been designed. The transition design is based on the work [16]. Nevertheless, a tuning for all the geometrical parameters are required in order to achieve a good transmission and reflection parameters in the desired frequency band and considering the designed SIW and the end-launch connector geometry. The transition design can be seen in Fig. 8 that shows low reflection and high transmission performance.

D. Simulated performance of array configurations

Finally, the directivity for all the array configurations is shown in Fig. 9. For these simulated results, the components described in subsection II. A are incorporated to the modular E-plane corporate feeding network of each array configuration. The simulated results reveal an impedance bandwidth performance below -10 dB for all the array configurations between 35 GHz to 41 GHz. It is interesting to point out that for the array configuration different from the single radiating layer case, the impedance bandwidth reaches up to 42 GHz. Moreover, in the array configuration with a single radiating layer, a high reflection is observed at 42 GHz. This is due to the existence of a strong resonance at this frequency in the waveguide component that uses the fragmented rectangular coupling aperture (see Fig. 7(c)). This fact causes a drop in the directivity at 42 GHz for the case of

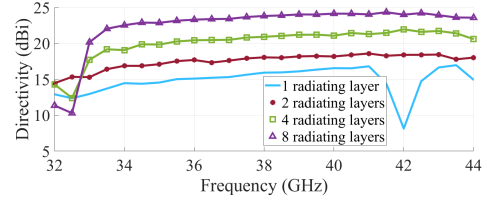


Fig. 9. Directivity of the different array configurations.

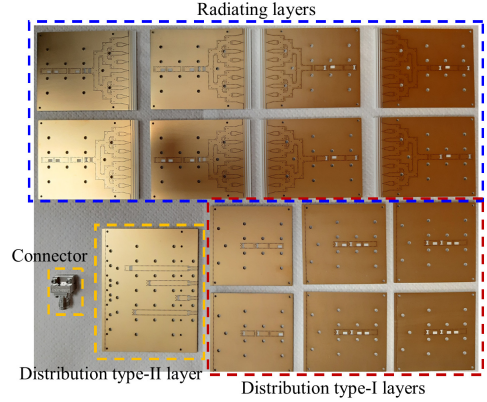


Fig. 10. End-launch connector and manufactured SIW layers that form all the possible array configurations.

the single radiating layer, which is observed in the Fig. 9. It is also shown how the directivity is enhanced when the number of radiating layer increases, producing a linear performance of the directivity in the desired frequency range for all the array configurations.

III. MEASUREMENTS AND DISCUSSION

The manufacturing and measurements of the modular SIW antenna array above described are presented in this section. Fig. 10 shows the manufactured SIW layers used in the assembly of all the possible array configurations. As can be seen in the figure, only three different types of SIW layers (radiating, distribution type-I and type-II) are required to manufacture. The layout of the distribution type-II layer can also be observed in Fig. 10. Four SIW lines with different lengths are implemented. At the end of each SIW lines, it is located the modified dog-bone coupling aperture used for the array configuration with 2, 4 and, 8 radiating layers while the rectangular coupling aperture is in one SIW line to the single radiating layer configuration. The reason for the different lengths of the SIW lines of the distribution type-II layer is because the position of the input of the E-plane distribution feeding network is different for each array configuration (see Fig. 5). A last geometric detail that can be appreciated in distribution type-II layer (also implemented in the distribution type-I layer) is a row of vias near the side of the layer. The implementation of these vias improves the directivity because they minimize the back radiation.

Before the radiation performance measurement of each array configuration, the dielectric losses are estimated. To calculate an estimation for the $\tan\delta$ value of the dielectric substrate, a measurement set-up similar to the one presented in [17] to estimate the insertion losses has been adopted. For our case, since we are dealing with SIW technology, the measurement set-up to calculate the insertion losses uses only the longest SIW line of the distribution type-II layer. In the measurement, the rectangular coupling aperture located at the end of the SIW line is short-circuited to produce a total reflection received by the end-launch connector placed at the other end of the SIW line. The expected $|S_{11}|$ value should be around 0 dB minus dielectric

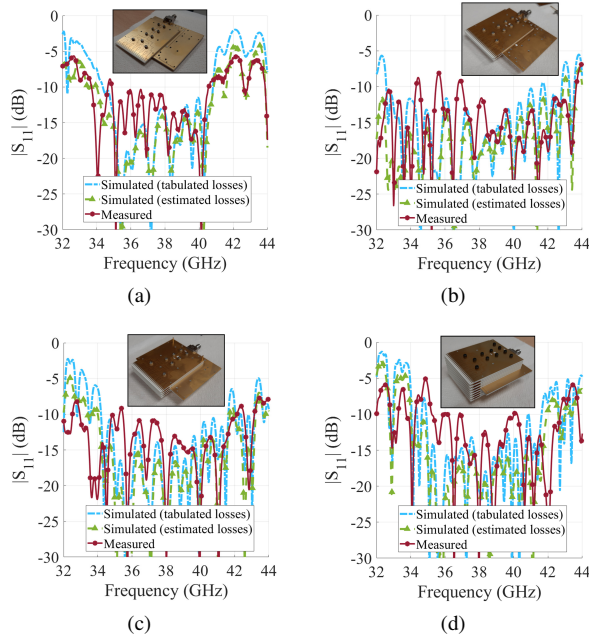


Fig. 11. Assembled modular arrays, simulated and measured $|S_{11}|$ for the different array configurations: (a) 1 radiating layer, (b) 2 radiating layers, (c) 4 radiating layers, and (d) 8 radiating layers.

losses that occur in the SIW line. For the simulation, a $\tan\delta$ value of 0.0067 has been set to match both simulated and measured results. This reveals a higher value than expected RO4003C so that it will produce higher dielectric losses in the corporate feeding networks.

The different array configurations are assembled as it is illustrated in insets of Fig. 11. The assembly screws have been placed close to the waveguide components to ensure electrical contact between layers and reduce leakage. In addition, some holes for alignment pins have been included in the corners of the plates to also reduce misalignment tolerances. The $|S_{11}|$ parameter has been measured for all the configurations. The VNA model used in all the measurement process is the R&S-ZVA67. Fig. 11 presents the simulated and measured results of each array configuration. The simulated results takes into account the estimated value for the $\tan\delta$ value. As can be seen there is a agreement between the measured and the simulated results. For all the array configurations, the measured impedance bandwidth is the one expected from 35 GHz to 41 GHz (15.79%).

Once the reflection coefficients are measured, the radiation performance is characterized in the anechoic chamber. Fig. 12 presents the simulated and measured results of the H- and E-plane radiation patterns at two different frequencies for the 1-radiating layer and 8-radiating layers configurations. Complementary, in Fig. 13, it is illustrated the 3-D radiation patterns of all the array configurations at the center frequency. Regarding Fig. 12, there is an adequate agreement between the simulations and the measurements with a stable radiation pattern shape along the frequency range. The H-plane radiation pattern is similar for both array configurations since the number of SIW horns is maintained along the H-plane of radiation. On the contrary, for the E-plane radiation patterns, it is observed a noticeable narrowing between both array configurations. This is due to the increase of antenna elements in the E-plane of radiation when the radiating layers are stacked. The straightforward consequence of this beam narrowing is a high increase in the directivity, as it was observed in Fig. 9. The progressive narrowing of the main beam in the E-plane can be seen in Fig. 13, where the intermediate configurations are shown. For the sake of brevity, only a single frequency is

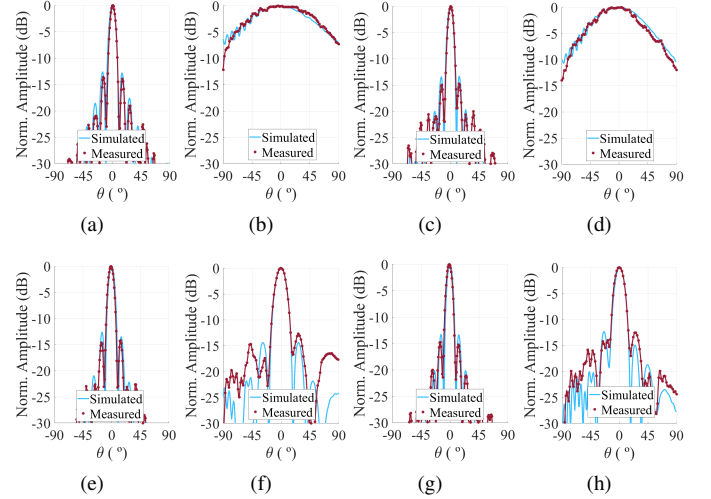


Fig. 12. Radiation patterns for the 1 radiating layer configuration: (a) H-plane and (b) E-plane at 36 GHz. (c) H-plane and (d) E-plane at 40 GHz. Radiation patterns for the 8 radiating layer configuration: (e) H-plane and (f) E-plane at 36 GHz. (g) H-plane and (h) E-plane at 40 GHz.

presented since the adequate performance of the radiation patterns along the frequency has been demonstrated in Fig. 12. There is some asymmetry in the E-plane radiation patterns because in this plane, the array configurations are not entirely symmetrical due to the presence of the connector on one side distribution type-II layer and the anchoring elements in the measurement setup. Additionally, some differences between simulated and measured results can be observed in secondary lobes (beyond 45°) mainly due to tolerances in the array assembly and measurement setup. Nevertheless, the measured main lobe is in good agreement with the simulated one and secondary lobes maintain the maximum level observed in simulation.

Fig. 14 shows the simulated and measured results of the realized gain for all the array configurations. It can be observed the agreement between the simulated and measured realized gain values for all the array configurations. There are some discrepancies between the simulated and measured values due to the loss tangent estimation and the small amount of power received outside the operating bandwidth. The realized gains are stable in the desired frequency band with some linear increase due to the increase of the electrical size of the aperture with frequency. Unfortunately, due to the high value of the $\tan\delta$ value, the realized gain values are not as high as expected and this fact is magnified as the E-plane corporate network gets larger. The simulated mean radiation efficiency in the operation bandwidth are 28.1%, 30.8%, 26.1% and 18.6% for each array configuration, from 1 to 8 radiating layers. Outside the operating frequency band, the realized gains drop due to impedance mismatching and dielectric losses. The cross polarization for all configurations is practically linear, obtaining values below -18.2 dB for cross-polarisation discrimination for any array configuration and operating frequency in the direction of maximum radiation.

Finally, the Table I discusses the novelty of this work in relation to other SIW antenna arrays at millimeter-wave frequencies. The works included in the comparison table are the most related ones that present a multilayer design with endfire radiation. In [8], a pyramidal horn antenna designed by stacking perforated SIW layers is presented. High radiation performance with low side lobe levels are achieved but in narrow bandwidth and without modularity. The authors in [18] introduce an array of 4 hollow SIW horn antennas with a high efficiency, but the modularity of the array design is limited. The work in [15] proposes a modular design of vertically stacked H-plane SIW

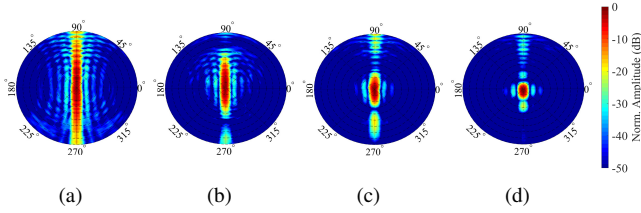


Fig. 13. Measured 3-D radiation pattern at 38 GHz: (a) 1 radiating layer, (b) 2 radiating layers, (c) 4 radiating layers, and (d) 8 radiating layers.

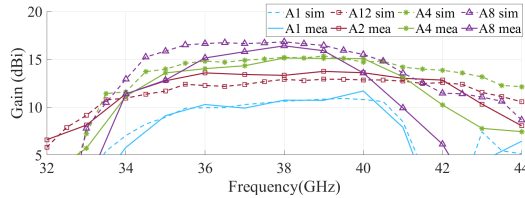


Fig. 14. Simulated and measured realized gain for all the array configurations.

horns. However, the design only offers two array configurations fed by a series coaxial feeding which produces a non-uniform feeding among the antenna elements. Moreover, some beam scanning is observed because of the modifications of the antenna phase feeding along the frequency. The proposed modular SIW antenna array avoids this beam-scanning problem because of the use of corporate feeding networks and also, it provides a great number of array configurations with a wider impedance bandwidth. Therefore, this modular SIW antenna array design provides a low-cost antenna solution due to its modularity to produce a certain directivity in the E-plane.

IV. CONCLUSIONS

This paper presents a fully modular SIW array design for millimeter-wave frequencies. By the use of modular corporate feeding network in the array design, all the antenna elements are fed uniformly in phase and amplitude. This keeps the main beam direction fixed along the frequency for all the 4 array configurations. Prototypes have been manufactured to validate the proposed modular array design. The measured results reveal a low reflection value and satisfactory radiation pattern performance for the use of all array configurations from 35 GHz to 41 GHz. A narrowing in the beamwidth of the E-plane is produced when a greater number of radiating layers are used. Nonetheless, due to the dielectric material used in the SIW, the realized gain is lower than expected but this can be enhanced using other dielectric material with lower loss tangent such as air, in a air-SIW design. The proposed modular array design is an advantage in a mass production situation because if the same number of multilayer arrays are needed but without modularity, a high number of different layers must be fabricated increasing the price.

REFERENCES

- [1] V. Chandrasekhar, J. G. Andrews, and A. Gatherer, "Femtocell networks: a survey," *IEEE Commun. Mag.*, vol. 46, no. 9, pp. 59–67, 2008.
- [2] Y. Hu, J. Zhan, Z. H. Jiang, C. Yu, and W. Hong, "An Orthogonal Hybrid Analog-Digital Multibeam Antenna Array for Millimeter-Wave Massive MIMO Systems," *IEEE Trans. Antennas Propag.*, vol. 69, no. 3, pp. 1393–1403, 2021.
- [3] R. M. Moreno, J. Ala-Laurinaho, and V. Viikari, "Plastic-Filled Dual-Polarized Lens Antenna for Beam-Switching in the *Ka*-band," *IEEE Antennas Wirel. Propag. Lett.*, vol. 18, no. 12, pp. 2458–2462, 2019.
- [4] F. Xu and K. Wu, "Guided-wave and leakage characteristics of substrate integrated waveguide," *IEEE Trans. Microw. Theory Techn.*, vol. 53, no. 1, pp. 66–73, 2005.

TABLE I
COMPARISON BETWEEN THE RELATED MULTILAYER SIW ARRAYS

Ref.	Frequency band (GHz)	Directivity (dBi)*	Aperture efficiency [†]	Modularity
[8]	35.1	14.6 ₈	73.84% ₈	No
[15]	32.9 - 37 (11.73%)	11 ₁ / 14 ₄	48.8% ₁ / 25.8% ₄	Yes (2 arrays)
[18]	27.6 – 38.1 (31.9%)	12 ₁ / 18 ₄	47.9% ₁ / 27.3% ₄	No
This work	35 - 41 (15.79%)	15.8 ₁ / 18.1 ₂ 20.9 ₄ / 23.8 ₈	66.6% ₁ / 56.6% ₂ 55.1% ₄ / 52.5% ₈	Yes (4 arrays)

* Simulated directivity at the center frequency.

[†] At the center frequency without considering the dielectric losses. Eq. (2) of [19] applied when two-dimensional aperture efficiency formula is greater than 1.

Note: The subscripts indicate the number of radiating layers in the array.

- [5] C. Di Paola, K. Zhao, S. Zhang, and G. F. Pedersen, "SIW multibeam antenna array at 30 GHz for 5G mobile devices," *IEEE Access*, vol. 7, pp. 73 157–73 164, 2019.
- [6] Q. Wu, J. Hirokawa, J. Yin, C. Yu, H. Wang, and W. Hong, "Millimeter-wave multibeam endfire dual-circularly polarized antenna array for 5G wireless applications," *IEEE Trans. Antennas Propag.*, vol. 66, no. 9, pp. 4930–4935, 2018.
- [7] Y. Cai, Y. Zhang, Z. Qian, and J. Liu, "A 16-element corporate-feed multilayer SIW cavity-backed slot antenna array," *IET Microw. Antennas Propag.*, vol. 11, no. 12, pp. 1796–1802, 2017.
- [8] L. Gong, Y. Fu, K. Y. Chan, J. A. Nanzler, and R. Ramer, "An SIW Horn Antenna Fed by a Coupled Mode Emulating Pyramidal Horn Antennas," *IEEE Trans. Antennas Propag.*, vol. 68, no. 1, pp. 33–42, 2020.
- [9] J.-W. Lian, Y.-L. Ban, Q.-L. Yang, B. Fu, Z.-F. Yu, and L.-K. Sun, "Planar Millimeter-Wave 2-D Beam-Scanning Multibeam Array Antenna Fed by Compact Siw Beam-forming Network," *IEEE Trans. Antennas Propag.*, vol. 66, no. 3, pp. 1299–1310, 2018.
- [10] R. W. Kindt, "Prototype Design of a Modular Ultrawideband Wavelength-Scaled Array of Flared Notches," *IEEE Trans. Antennas Propag.*, vol. 60, no. 3, pp. 1320–1328, 2012.
- [11] J. T. Logan, R. W. Kindt, M. Y. Lee, and M. N. Vouvakis, "A New Class of Planar Ultrawideband Modular Antenna Arrays With Improved Bandwidth," *IEEE Trans. Antennas Propag.*, vol. 66, no. 2, pp. 692–701, 2018.
- [12] C.-N. Chen *et al.*, "38-GHz Phased Array Transmitter and Receiver Based on Scalable Phased Array Modules With Endfire Antenna Arrays for 5G MMW Data Links," *IEEE Trans. Microw. Theory Techn.*, vol. 69, no. 1, pp. 980–999, 2021.
- [13] R. Klimovich, S. Jameson, and E. Socher, "W-Band Endfire 2-D Phased-Array Transmitter Based on $\times 9$ CMOS Active Multiplier Chips," *IEEE Trans. Antennas Propag.*, vol. 68, no. 12, pp. 7893–7904, 2020.
- [14] N. Memeletzoglou and E. Rajo-Iglesias, "Array of stacked leaky-wave antennas in groove gap waveguide technology," *Sci. Rep.*, vol. 11, 01 2021.
- [15] C. Segura-Gómez, Á. Palomares-Caballero, A. Alex-Amor, J. Valenzuela-Valdés, and P. Padilla, "Modular Design for a Stacked SIW Antenna Array at Ka-Band," *IEEE Access*, vol. 8, pp. 158 568–158 578, 2020.
- [16] R. Kazemi, A. E. Fathy, S. Yang, and R. A. Sadeghzadeh, "Development of an ultra wide band GCPW to SIW transition," in *2012 IEEE Radio and Wireless Symposium*, 2012, pp. 171–174.
- [17] Á. Palomares-Caballero, A. Alex-Amor, J. Valenzuela-Valdés, and P. Padilla, "Millimeter-Wave 3-D-Printed Antenna Array Based on Gap-Waveguide Technology and Split E-Plane Waveguide," *IEEE Trans. Antennas Propag.*, vol. 69, no. 1, pp. 164–172, 2021.
- [18] Z. Qi, X. Li, J. Xiao, and H. Zhu, "Dielectric-slab-loaded hollow substrate-integrated waveguide *h*-plane horn antenna array at *ka*-band," *IEEE Antennas and Wireless Propagation Letters*, vol. 18, no. 9, pp. 1751–1755, 2019.
- [19] L. Dai, Y. Xie, H. Wang, and P. Wu, "Three-dimensional aperture principle for end-fire radiation antenna array," *AIP Advances*, vol. 11, no. 2, p. 025116, 2021.